Hydrothermal Splitting of Titanate Fibers to Single-Crystalline TiO₂ Nanostructures with Controllable Crystalline Phase, Morphology, Microstructure, and Photocatalytic Activity

Liming Shen,[†] Ningzhong Bao,*,[†] Yanqing Zheng,[‡] Arunava Gupta,[†] Taicheng An,[§] and Kazumichi Yanagisawa[‖]

Center for Materials for Information Technology, The University of Alabama, Tuscaloosa, Alabama 35487, Shanghai Institute of Ceramics, Chinese Academy of Sciences, Shanghai 201800, China, Guangzhou Institute of Geochemistry, Chinese Academy of Science, Guangzhou 510640, China, and Research Laboratory of Hydrothermal Chemistry, Kochi University, Kochi 780-8520, Japan

A simple and efficient inorganic acid-assisted hydrothermal route has been developed for the synthesis of single-crystalline TiO₂ nanostructures with use of protonic tetratitanate hydrate fibers as a precursor. A variety of TiO₂ nanostructures, including aligned nanorods, nanoporous nanostructures, nanocubes, and diamond-shaped nanocrystals, have been prepared with this method. The morphology, crystalline phase, composition, average grain size, band gap, and microstructure of the nanostructures have been determined as a function of the nature and concentration of the inorganic acid (HCl, HNO₃, or H₂SO₄) used for the synthesis. The rutile phase is obtained by using HCl for a concentration range of 0.1−0.4 M and also for 6 M concentration, HNO₃ for a concentration range of 0.1−0.2 M and >7 M, and H₂SO₄ for a narrow concentration range of 0.1−0.9 M. Likewise, the anatase phase is obtained by using both HCl and HNO₃ for concentrations of around 0.9 M, and a broader concentration range of 2−7 M with H₂SO₄. An increase in the band gap of the TiO₂ nanostructures from 2.97 to 3.35 eV is observed as the crystalline phase changes from rutile, to a mixture of rutile and anatase, and subsequently to pure anatase. Correspondingly, the photocatalytic activity of the synthesized nanostructured materials is found to be dependent on the crystalline phase, composition, and surface area.

1. Introduction

TiO₂ is an important semiconductor material for use in a wide range of applications, including photocatalysis, environmental pollution control, and solar energy conversion. In particular, various nanocrystalline forms of TiO₂ have been intensively studied in recent years since their physical and chemical properties have been found to be superior to those in the bulk.[1–4] The properties of nanocrystalline TiO₂ are determined by a variety of factors, including their shape, size, crystallinity, phase, composition, etc. Building on to the extensive work on spherical nanoparticles, the assembly of shape-controlled nanostructure has recently been gaining importance, both for fundamental scientific research and technological applications. This is because of the richness of the anisotropic structures and properties offered by the complex shapes.[5–9] For example, the electron transport in single-crystalline TiO₂ nanowires is expected to be several orders of magnitude faster than percolation through a random polycrystalline network, which is very relevant for improving the photocatalyic efficiency of the semiconductors for solar energy conversion.[10]

The majority of the applications of TiO₂ are also influenced by the crystalline phase.[11] TiO₂ has three primary crystalline forms: anatase, rutile, and brookite, with the anatase and rutile phases being the most intensively investigated phases.[12] Ther-

modynamically, the rutile phase is more stable than anatase,[13] and has been widely used because of its chemical stability and high refractive index.[14] However, the anatase phase exhibits better efficiency for photocatalysis and solar energy conversion.[15] Mixtures of the rutile and anatase have been found to exhibit catalytic reaction efficiency, which is dependent on the relative ratio of the two phases.[16,17] Novel properties and applications of TiO₂ nanomaterials can be expected if the crystalline phase and composition of the shape-controlled nanocrystal assemblies can be simultaneously controlled.

To assemble shape-controlled TiO₂ nanocrystals, a variety of multistep procedures, including solvent evaporation of colloid crystal solutions,[18] template-directed synthesis,[19] etc., have been developed. However, all these procedures require uniform nanoparticles as a starting material. While well-controlled aligned TiO₂ nanotube/nanorod arrays have been prepared by methods such as anodic oxidation of metal Ti foils in fluorine-containing electrolytes,[20,21] electrophoresis,[22] etc., the as-synthesized products are amorphous. For controlling the crystalline phase and composition of the TiO₂ materials from solution at room temperature, a specific aging time is often necessary to obtain either the pure anatase or the anatase−rutile phase mixture. While the direct formation of the rutile phase requires aging for days or even longer,[23–25] calcination of amorphous TiO₂ nanotube/nanorod arrays generates anatase, and a mixture of anatase and rutile within several hours. However, obtaining pure rutile requires calcinations at temperatures higher than 500 °C, which often results in the collapse of nanotube/nanorod arrays and formation of a polycrystalline structure. Thus, the development of a simple and cost-effective synthesis route for the large-scale production of single-crystalline nano-

* Corresponding author. Phone: 205-348-5041. Fax: 205-348-9104. E-mail: nzhbao@mint.ua.edu.
† Center for Materials for Information Technology, The University of Alabama.
‡ Shanghai Institute of Ceramics, Chinese Academy of Sciences.
§ Guangzhou Institute of Geochemistry, Chinese Academy of Science.
‖ Research Laboratory of Hydrothermal Chemistry, Kochi University.

structures of assembled shape-controlled TiO$_2$nanocrystals, with tunable crystalline phase and phase composition, will represent a significant step for realizing novel applications of TiO$_2$ nanomaterials.

The large-scale preparation of nanocrystalline TiO$_2$ has thus far been achieved either by the direct hydrolysis of inorganic titanium salts or organometallic precursors in solvents at room temperature or above under hydrothermal condition.[26–36] Chemical conversion of some amorphous or hydrous titania and titanates to nanocrystalline TiO$_2$ has also been reported.[37–46] The nature of the precursor used for the syntheses often plays a key role in determining the formation and crystallization of the TiO$_2$ nanocrystallites. The formation and organization of the titanium polynuclear complexes needed for the nucleation and growth of various forms of TiO$_2$ is determined by both the anionic species and the acidity of the solution.[32–36] The commonly used titanium precursors are either inorganic salts, such as TiCl$_4$ and TiOSO$_4$, or organometallic compounds such as titanium acetylacetonate and titanium isopropoxide, which are usually quite expensive, corrosive, and sensitive to moisture. Moreover, complex nanostructures of assembled TiO$_2$ nanocrystals are usually difficult to obtain from these titanium precursors. On the other hand, the use of some amorphous titania and titanate hydrates precursors has been found to have a significant influence on both the phase formation and crystal growth of various TiO$_2$ products.[37–39] For example, relatively modest reaction temperatures and short reaction times are needed for the reaction by replacing crystalline reactants with amorphous titania hydrate precursors.[40–42] However, the morphology of the products is completely different from that of the reactants. But it is possible to preserve the morphology and structure of the solid titanate precursors by using suitable conditions during the phase formation and transformation reactions.[41–49] TiO$_2$ with different crystal phases, morphologies, and microstructures has been prepared from protonic titanate hydrates by either calcination or hydro/solvothermal reactions.[50–53] This is due to the fact that protonic titanates are a group of solid TiO$_2$ hydrates with layered crystal structure intercalated by protonated water molecules. Each layer in the crystal structure consists of side-by-side aligned TiO$_6$ octahedra connected above and below by additionally shared apical edges of TiO$_6$ octahedra at different levels.[41–49] The layers within the titanate hydrates can either split into smaller fragments of TiO$_6$ octahedra for use in the assembly of more complex nanostructures, or can dehydrate in situ and crystallize. This is different from the growth of rutile or anatase phases from polymorphic growth units formed from Ti^{4+}or organometallic titanium compounds by hydrolysis.[42–45,52,53] This possibility opens a new route that is capable of assembling novel complex TiO$_2$ nanostructures by using relatively large TiO$_2$ nanoblocks formed by self-splitting of the titanate hydrates.

In the present study, we report on a simple and efficient inorganic acid-assisted hydrothermal synthesis strategy for the direct preparation of single-crystalline TiO$_2$ nanostructures. Our synthesis route involves use of stable, nontoxic, air/moisture-insensitive synthetic precursors of protonic tetratitanate hydrate fibers. The morphology, microstructure, crystalline phase, band gap, and phase composition of the synthesized TiO$_2$ nanostructures can be easily controlled by changing the nature and concentration of the inorganic acid used for reaction. A wide variety of aligned nanorods, nanoporous nanorods, nanocubes, and diamond-shaped nanocrystals have been obtained with our synthesis route. Using methyl orange as a model compound, we have evaluated the photocatalytic activity of the nanocrystalline TiO$_2$ products using Degussa P-25 as a reference standard.

2. Experimental Section

Synthesis of Protonic Tetratitanate Hydrate Fibers. K$_2$Ti$_4$O$_9$ fibers were prepared by calcination of a mixture of hydrous titanium dioxide and K$_2$CO$_3$, with a TiO$_2$/K$_2$O molar ratio of 3.0, at 1000 °C for 2 h. Protonic tetratitanate hydrate fibers with the chemical formula H$_2$Ti$_4$O$_9$·1.2H$_2$O were then obtained through three cycles of ion exchange of 1 g of K$_2$Ti$_4$O$_9$ fibers in 500 mL of 0.1 M HCl solution. The product was washed with water and ethanol several times, and then dried in a vacuum oven for 24 h at 60 °C.

Hydrothermal Synthesis Reactions. Inorganic aqueous acid solutions of different concentrations, including 0.1−6 M HCl, 0.1−10 M HNO$_3$, and 0.1−7 M H$_2$SO$_4$, were initially prepared. Subsequently, 1 g of protonic tetratitanate hydrate fibers was dispersed in 60 mL of each of the inorganic acid solutions with stirring for 24 h, and then transferred into the 80 mL container of a Teflon-lined stainless steel autoclave. After adequate sealing, the autoclave was heated and maintained at 150 °C for 24 h, and then cooled to room temperature. The precipitate was collected, centrifuged, washed with distilled water and ethanol several times, and then dried overnight in a vacuum oven at 60 °C.

Characterization of the Materials. Powder X-ray diffraction (XRD) patterns were obtained with a Rigaku Rotaflex type X-ray diffractometer. Cu Kα radiation with a nickel filter, operating at 40 kV and 100 mA, was used as the source. All the samples were measured in the continuous scan mode in the 2θ range of 15−55°, using a scan rate of 0.02 deg/s. The peak positions and relative intensities of the product peaks were characterized by comparing with the standard Joint Committee for Powder Diffraction Standards (JCPDS) data. The crystalline domain size was calculated from the full width at half-maximum (fwhm, in radians), using the Scherrer's formula $D = 0.9\lambda/(\beta \cos\theta)$, where λ is the employed X-ray wavelength, θ is the diffraction angle of the most intense diffraction peak, and β is defined as the half-width after subtracting the instrumental broadening.[54,55] The morphology and structure of the products were observed with transmission electron microscopy (TEM) capable of high resolution (HR) (Tecnai F-20), operating at 200kV. A NOVA 1200e, surface area and pore size analyzer, was employed to obtain N$_2$ adsorption/desorption isotherms of some of the prepared samples. The BET specific surface area was calculated in a relative pressure range of $0.05 < P/P_0 < 0.2$. The t-plot method was used to calculate the micropore (<1 nm) surface area. Main diameter distributions, surface areas, and pore volumes of mesopores (>2 nm) were calculated from N$_2$ desorption isotherms by the BJH method. The optical absorption spectra were obtained with an Ultraviolet−Visible diffuse reflectance spectrometer (UV−vis DRS, V-560, JASCO).

Evaluation of Photocatalytic Activity. Photocatalytic reactions were carried out on stirred suspensions at 25 °C in a 530 mL Pyrex reactor. A 300 mL solution containing 20 mg·L^{-1} of methyl orange and 0.5 g·L^{-1} of the catalyst was air equilibrated and stirred at 800 rpm for 10 min before irradiation by a 450 W Hg lamp. The pH value of reaction solution was maintained at 3.0 by addition of concentrated HNO$_3$ solution. During the reaction process, a small amount of the solution was withdrawn intermittently for analysis, and the methyl orange concentration was determined by measuring the absorbance at 480 nm, using the UV−vis spectrophotometer. The apparent
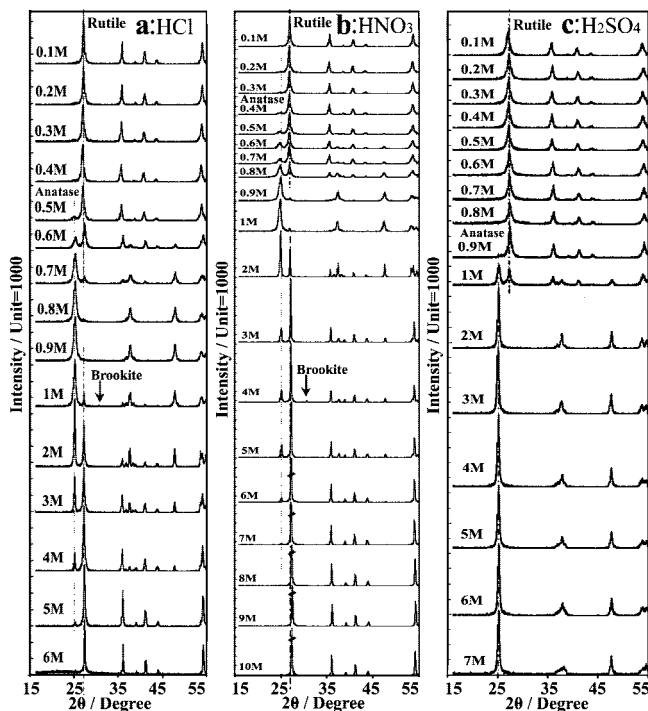
Hydrothermal Splitting of Titanate Fibers

J. Phys. Chem. C, Vol. 112, No. 24, 2008 **8811**

Figure 1. XRD patterns of hydrothermally synthesized TiO_2 products from protonic tetratitanate hydrate fibers in acidic solutions of (a) 0.1−6 M HCl, (b) 0.1−10 M HNO_3, and (c) 0.1−7 M H_2SO_4.

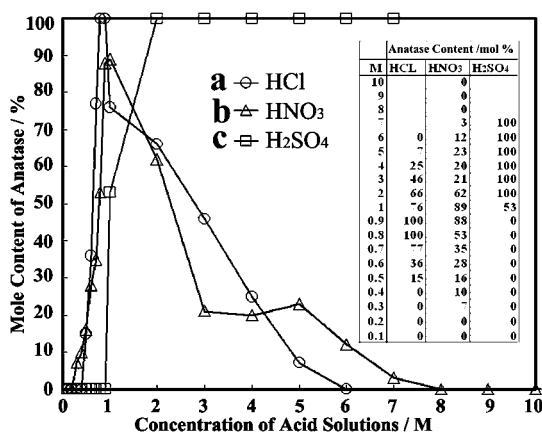| Anatase Content /mol %			
M	HCL	HNO3	H2SO4
10		0	
9		0	
8		0	
7		3	100
6	0	12	100
5	7	23	100
4	25	20	100
3	46	21	100
2	66	62	100
1	76	89	53
0.9	100	88	0
0.8	100	53	0
0.7	77	35	0
0.6	36	28	0
0.5	15	16	0
0.4	0	10	0
0.3	0	7	
0.2	0	0	
0.1	0	0	

Figure 2. Acid concentration dependence of the ratio of anatase in the products hydrothermally synthesized with use of (a) HCl, (b) HNO_3, and (c) H_2SO_4, respectively. The anatase component is determined as (100% rutile). The inset presents numerical values of all the data points in the figure.

Figure 3. Acid concentration dependence of the average grain sizes of the products hydrothermally synthesized with use of (a) HCl, (b) HNO_3, and (c) H_2SO_4, respectively.

reaction rate constant, for determining the photocatalytic activity, was calculated based on the photodegradation data of a 10-min photocatalytic reaction. Degussa P-25, a commonly used standard in photocatalysis studies, was used to evaluate the relative photocatalytic activities of our samples.

3. Results and Discussion

3.1. Materials Characterization and Properties of TiO_2 Nanostructures. *Phase Structure and Composition of the TiO_2 Products.* The phase composition and purity of all the products have been identified based on the respective XRD patterns, shown in Figure 1. The anatase phase content for all the products has been calculated from the corresponding XRD patterns, as shown in Figure 2. The products have been confirmed to be primarily anatase, rutile, or a mixture of anatase and rutile. The minority brookite phase has been observed only in the products
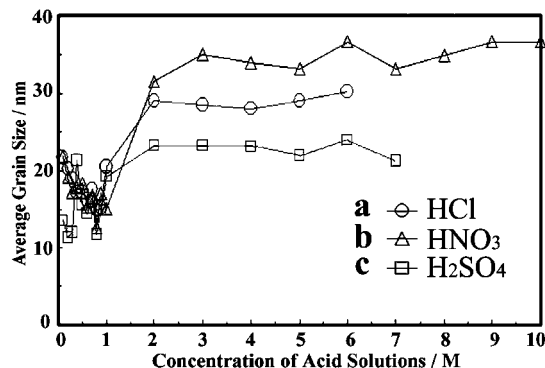
synthesized with 1 M HCl and 4 M HNO_3. As shown in Figure 2a, with increasing concentration of HCl the obtained products are found to be pure rutile for <0.5 M, a mixture of rutile and anatase for 0.5−0.8 M, pure anatase for 0.9 M, a mixture of rutile and anatase for 1.0−6 M, and again pure rutile for 6 M. On the other hand, as seen in Figure 2b, with increasing concentration of HNO_3, the obtained products are pure rutile for <0.4 M, a mixture of rutile and anatase for 0.4−7 M, and pure rutile for >7 M. The anatase content reaches a maximum value of 90% in the products obtained with a HNO_3 concentration of 0.9−1.0 M. Finally, as shown in Figure 2c, with increasing concentration of H_2SO_4, the obtained products are pure rutile for <0.9 M, a mixture of rutile and anatase for 0.9−2 M, and pure anatase for >2 M. Thus, a mixture of rutile and anatase with a continuously changing ratio is obtained over a wide concentration range of 0.4−7 M for both HCl and HNO_3, but only a narrow concentration range of 1−2 M for H_2SO_4. However, either the pure anatase or rutile phase can be obtained with H_2SO_4 over a wide concentration range.

Average Grain Size of the TiO_2 Products. Average grain sizes of all the products have been estimated from the full width at half-maximum (fwhm, in radians) of the respective XRD patterns with the Scherrer's formula. As shown in Figure 3a, with increasing concentration of HCl, the average grain size of the product decreases from 22 nm for 0.1 M to 14 nm for 0.8 M, and then increases to about 29 nm for 2.0 M. The average grain size further increases slightly for >2.0 M and achieves a maximum value of about 30 nm for 6 M HCl in our experiments. The products prepared in HNO_3 exhibit a similar tendency for the average grain size. As shown in Figure 3b, the average size of the products decreases from 22 to 13 nm with increasing the concentration of HNO_3 from 0.1 to 0.8 M, and then increases rapidly to 35 nm when reaching a concentration of 3.0 M. The average grain size then varies between 35 and 37 nm for 4−10 M HNO_3. For the products prepared in H_2SO_4, as shown in Figure 3c, the average grain size varies between 11 and 21 nm for a H_2SO_4 concentration of <1.0 M, and maintains a stable value as the concentration of H_2SO_4 is increased to >2.0 M. It should be noted that the average grain size of the products obtained in H_2SO_4 is comparatively smaller than those obtained in reaction with HCl and HNO_3.

Shape and Microstructure of the TiO_2 Products. The morphology and structure of the obtained TiO_2 products has been investigated by transmission electron microscopy (TEM) and high-resolution TEM (HRTEM). $K_2Ti_4O_9$ fibers (Figure 4a) are used to prepare $H_2Ti_4O_9 \cdot 1.2H_2O$ fibers (Figure 4b) by the controlled ion exchange reaction, in which both $K_2Ti_4O_9$ and $H_2Ti_4O_9 \cdot 1.2H_2O$ maintain the same fibrous morphology of
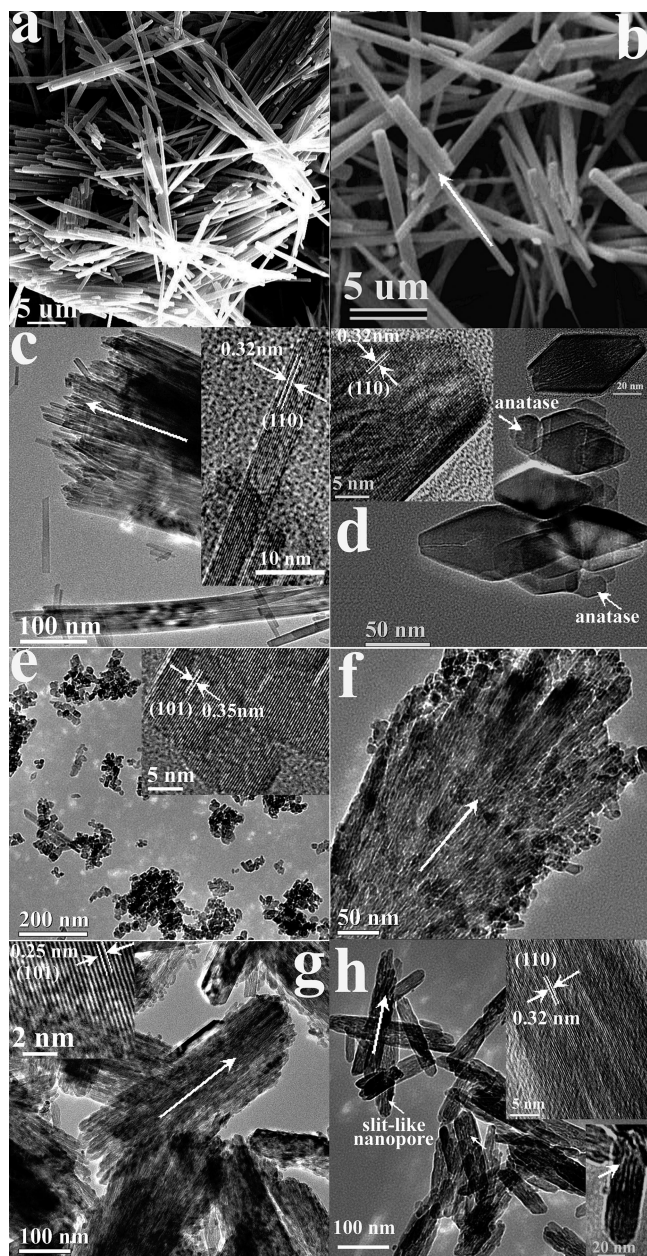
Figure 4. (a) SEM images of $K_2Ti_4O_9$ and (b) protonic tetratitanate hydrate $H_2Ti_4O_9 \cdot 1.2H_2O$ fibers. TEM images of TiO_2 nanostructures hydrothermally synthesized in HCl: (c) aligned rutile ultralong nanorods (in 6 M HCl); (d) a mixture of diamond-shaped rutile and spherical anatase nanocrystals (in 3 M HCl); (e) anatase nanocrystals (in 0.8 M HCl); (f) a mixture of aligned rutile nanorods and anatase nanocrystals (in 0.6 M HCl); (g) aligned rutile short nanorods (in 0.4 M HCl); (h) porous rutile nanorods with slit-like nanopores indicated by the arrows and clear crystal lattice fringes indicated by the inset HRTEM image, prepared in 0.1 M HCl. All the TiO_2 products exhibit single crystalline structure as indicated by the inset HRTEM images to panels c, d, e, and g. A single rutile crystallite with a diamond shape is shown in the inset to panel d. The long arrows in panels b, c f, g, and h indicate the axial direction of original protonic tetratitanate fibers.

about $0.5-1$ μm in diameter and a length of dozens of micrometers. As shown in Figures 46, different single-crystalline TiO_2 nanostructures, such as aligned rutile/anatase nanorods, nanoporous rutile/anatase nanorods, anatase nanocubes, and diamond-shaped rutile nanocrystals, are obtained from the hydrothermal reaction of $H_2Ti_4O_9 \cdot 1.2H_2O$ fibers with HCl, HNO_3, or H_2SO_4 of different concentration.

The TiO_2 products synthesized with use of HCl show various morphologies and structures depending on the concentration of

HCl. As shown in Figure 4c, radially aligned long rutile nanorods, with a uniform diameter of around 5 nm and lengths of up to several micronmeters, are obtained in 6 M HCl, which assemble to form nanostructures of several hundreds of nanometers in diameter and several micrometers in length. The HRTEM image (shown as an inset in Figure 4c) of an individual nanorod shows clear crystal lattice fringes with interlayer distances measured to be 0.32 ± 0.002 nm, close to the 0.325 nm lattice spacing of the (110) planes in rutile TiO_2, which indicates the single crystalline structure of the rutile nanorods. A mixture of rutile and anatase is formed for HCl concentrations of $0.9-6$ M. A typical product (Figure 4d), prepared hydrothermally in 3 M HCl, consists of diamond-shaped rutile and spherical anatase nanocrystals as identified with arrows. The ratio of the rutile to anatase in the product decreases with decreasing concentration of HCl. As shown in Figure 4e, pure anatase nanocrystals, with an average size of about 10 nm, are obtained for a HCl concentration of 0.8 M. The HRTEM image of several anatase nanocrystals (shown as an inset in Figure 4e) shows lattice fringes with an interlayer distance of 0.35 nm, close to the 0.352 nm lattice spacing of the (101) planes in anatase TiO_2. However, pure anatase can be obtained by using HCl only over a very narrow concentration range of around 0.8 M. With further reduction of the HCl concentration, a mixture of rutile and anatase appears for 0.7 M, and the anatase fraction disappears completely for 0.5 M. As shown in Figure 4f, the products prepared in 0.6 M HCl are composed of aligned rutile nanorods in which anatase nanoparticles occupy almost all of the spaces within the aligned rutile nanorods. Both the anatase nanoparticles and the rutile nanorods formed within the protonic tetratitanate hydrate ($H_2Ti_4O_9 \cdot 1.2H_2O$) fibers are maintained without reorganization, but the whole $H_2Ti_4O_9 \cdot 1.2H_2O$ fibers can collapse into small pieces because of dehydration and crystal lattice rearrangement. This results in the formation of TiO_2 nanostructures of about 250 nm in diameter and several micrometers in length. With further decreasing the concentration of HCl below 0.5 M, only rutile nanorods, as shown in Figure 4g,h, are observed. Aligned short rutile nanorods (Figure 4g) of about 12 nm in diameter and up to about 800 nm in length are obtained with 0.4 M HCl. Porous rutile nanorods (Figure 4h), with diameters of $20-40$ nm and lengths of up to about 200 nm, are obtained with 0.1 M HCl. Slit-like pores (the inset to Figure 4h) of about 2 nm in width are observed. All the rutile nanorods are single-crystalline structures as indicated by the representative HRTEM images.

The variations in the morphology and structure of the TiO_2 products hydrothermally synthesized with HNO_3 are similar to the products prepared with HCl. As shown in Figure 5a, rutile nanorods, with diameters in the range of $30-80$ nm and lengths of up to several micronmeters, are obtained with $8-10$ M HNO_3. The rutile nanorods are radially aligned to form nanostructures of $300-500$ nm in diameter and $0.5-2$ μm in length. As shown in Figure 5b,c, a mixture of rutile and anatase is obtained with $2-7$ M HNO_3. Anatase nanocubes with sizes of about $50-100$ nm exist in all the products. However, rutile nanorods are observed only in the products obtained with $3-7$ M HNO_3. With further decreasing the concentration of HNO_3 to $1-2$ M, the products are diamond-shaped rutile nanocrystals with an average size of about 80 nm, which is the same as those shown in Figure 4d. A maximum anatase content of about 90% has been determined in the products prepared with 1 M HNO_3 (Figure 5c). As shown in Figure 5d, anatase nanocrystals occupy all the space existing between the aligned rutile nanorods, forming nanostructures with a large size of about 20 nm in diameter
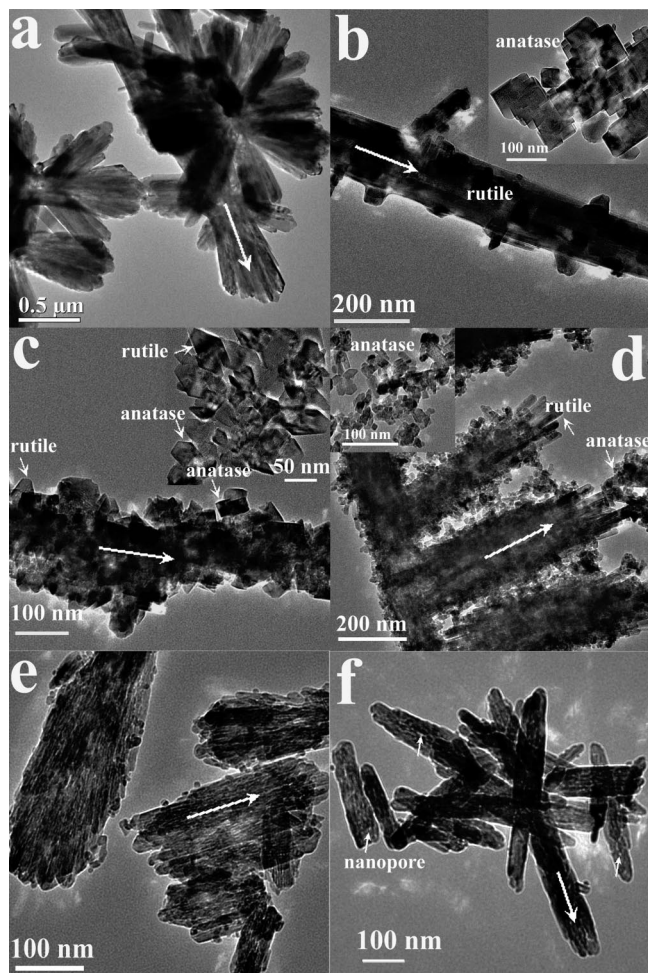
Figure 5. TEM images of TiO$_2$ nanostructures hydrothermally synthesized in HNO$_3$ solution: (a) aligned rutile long nanorods (in 6 M HNO$_3$); (b) a mixture of anatase nanocubes and rutile nanorods (in 3 M HNO$_3$); (c) a mixture of anatase nanocubes and diamond-shaped rutile nanocrystals (in 1 M HNO$_3$); (d) a mixture of aligned rutile nanorods and anatase nanocrystals indicated by the inset TEM image (in 0.8 M HNO$_3$); (e) aligned rutile short nanorods (in 0.3 M HNO$_3$); and (f) porous rutile nanorods (in 0.1 M HNO$_3$). The longest arrows in panels a–f indicate the axial direction of the original protonic tetratitanate fibers.

Figure 6. TEM images of TiO$_2$ nanostructures hydrothermally synthesized in H$_2$SO$_4$ solution: (a1, a2) aligned nanoporous anatase nanorods (in 7 M H$_2$SO$_4$); (b) mixture of aligned rutile nanorods and anatase nanocrystals (in 1 M H$_2$SO4); (c) aligned rutile short nanorods with slit-like nanopores indicated by the inset magnified TEM images and continuous crystal lattice for a single nanorod indicated by the inset HRTEM image (in 0.9 M H$_2$SO$_4$). The longest arrows in panels a–c indicate the axial direction of original protonic tetratitanate fibers.

and 500–800 nm in length, which is similar to those shown in Figure 4f. By further decreasing the concentration of HNO$_3$ to 0.3 M, the anatase phase in the products disappears, and only aligned short nanorods (Figure 5e) are observed. Much shorter porous rutile nanorods (Figure 5f), with diameters of 20–50 nm and a length of up to about 500 nm, are obtained with 0.1 M HNO$_3$. The HRTEM images (not shown) of all products prepared with HNO$_3$ show clear lattice fringes, indicating their single-crystalline nature.

The TiO$_2$ products prepared in H$_2$SO$_4$ exhibit different structure and morphology as compared to the TiO$_2$ products prepared in HCl and HNO$_3$. As shown in Figure 6a1, radially aligned anatase nanorods of around 8 nm in diameter and 200–400 nm in length are obtained with 7 M H$_2$SO$_4$. Slit-like pores of about 4 nm in width are observed within the spaces between adjacent nanorods. Moreover, it is notable that nanopores with a diameter of 4–5 nm are observed within each individual nanorod (Figure 6a2). With a decrease in the concentration of H$_2$SO$_4$ to 1 M, the product is a phase mixture in which the anatase nanoparticles and aligned rutile nanorods are well arranged to form nanostructures of about 100–160 nm
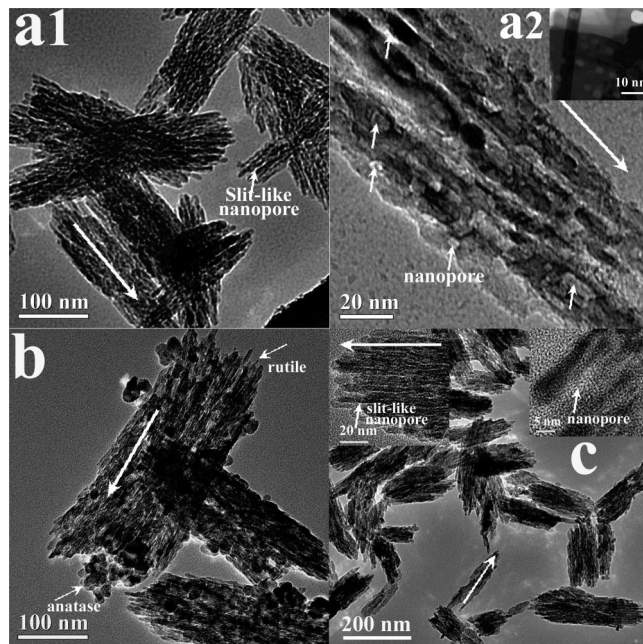
in diameter and up to 400 nm in length. By further decreasing the concentration of H$_2$SO$_4$ to 0.1–0.9 M, rutile nanorods (Figure 6c) containing uniformly distributed slit-like pores are formed. These rutile nanorods, with an average length of about 200 nm and average diameter of about 5 nm, are radially aligned to form porous nanostructures with lengths of about 200 nm and a diameter of about 80 nm.

The surface areas and pore structure properties of typical samples were determined by the N$_2$ adsorption/desorption isotherms. As shown in Table 1, the products synthesized in HCl show various surface areas and pore structures obviously depending on the shape, size, and structure of the TiO$_2$. Both the rutile nanorods (Figure 4c) and the mixture of diamond-shaped rutile nanoparticles and spherical anatase nanocrystals (Figure 4d) have small surface areas (about 16.5 and 18.1 m$^2 \cdot$g^{-1}, respectively) because of relatively large sizes. The anatase nanocrystals (Figure 4e) have the smallest size of about 14.9 nm, and thus exhibit the largest surface area of about 75.7 m$^2 \cdot$g^{-1}. In contrast, the surface areas of the mixture of rutile nanorods and anatase nanocrystals (Figure 4f) and the rutile nanorods (Figure 4g) are about 61.1 and 68.9 m$^2 \cdot$g^{-1}, respectively, which decrease a little because of relatively large size of the formed rutile nanorods. The sizes of the rutile nanorods, as shown in panels g, h, and c of Figure 4, increase, and thus their surface areas decease. Furthermore, since the size of all the rutile nanorods is larger than those of the anatase nanocrystals (Figure 4e,f), all the surface areas of the rutile nanorods are relatively smaller than those of the products containing anatase nanocrystals (Figure 4e,f). It is interesting that micropores are detected within the products containing rutile nanorods (Figure 4c,f,h), but none was found within the anatase nanocrystals (Figure 6e), which indicates that the rutile nanorods (Figure 4f,h) contain micropores.

TABLE 1: Chemical Component, Materials Characteristics, and Photocatalytic Activities of the Samples[a]

samples		constitute (%) Anatase	Rutile	ave grain size (nm)	band gap (eV)	surface areas and pore properties a	b	c	d	morphology	e
Figure	4e	100	0	14.9	3.35	75.7	0	67.8	0.29	nanocrystal	0.078
Figure 6a1−2		100	0	25.0	3.30	84.6	0	78.1	0.32	aligned nanoporous nanorod	0.071
Figure	4f	37	63	16.2	3.14	61.1	9.8	48.6	0.16	anatase nanocrystal rutile nanorods	0.045
Figure	6b	53	47	19.2	3.22	98.3	13.9	66.0	0.28	anatase nanocrystal rutile nanorods	0.057
Figure	5b	22	78	35.0	3.12	10.8	0	5	0.03	anatase nanocubes rutile nanorods	0.041
Figure	5c	90	10	15.1	3.30	48.7	0	35.3	0.13	anatase nanocubes diamond-like rutile nanocrystal	0.065
Figure	4d	44	56	23.3	3.10	18.1	0	15.1	0.09	spherical anatase nanocrystal diamond-like rutile nanocrystal	0.049
Figure	4c	0	100	30.2	2.99	16.5	2.10	12.9	0.05	aligned ultralong nanorod	0.021
Figure	4g	0	100	17.1	3.16	58.9	14.6	37.7	0.11	aligned short nanorod	0.025
Figure	4h	0	100	21.7	3.13	38.6	2.8	28.6	0.15	aligned nanoporous nanorod	0.038
P-25		70	30	20	3.01	50.2				nanoparticle	0.085

[a] a: BET surface area ($m^2 \cdot g^{-1}$). b: surface area ($m^2 \cdot g^{-1}$) of micropores (<1 nm) calculated by the t-plot method. c and d, respectively: surface area ($m^2 \cdot g^{-1}$) and pore volume ($cm^3 \cdot g^{-1}$) of mesopores (>2nm) calculated from N_2 desorption isotherms by the BJH method. e: apparent reaction rate constant (min^{-1}).

Some products synthesized in HNO_3 are the mixture of big rutile rods and anatase nanocubes (Figure 5b), showing the smallest surface area of about 10.8 $m^2 \cdot g^{-1}$. The mixture of anatase nanocubes and diamond-shaped rutile nanocrystals (Figure 5c) exhibits a small average gain size (15.1 nm), which is comparable to that of the anatase nanocrystals shown in Figure 4e. However, its surface area (about 48.7 $m^2 \cdot g^{-1}$) is not very high because the sticking of nanoparticles decreases the exposed surface area. For other products synthesized in H_2SO_4, nanoporous anatase nanorods (Figure 6a1,a2) and the mixture of aligned short rutile nanorods and anatase nanocrystals (Figure 6b) exhibit very large surface areas of 84.6 and 98.3 $m^2 \cdot g^{-1}$, respectively, since the former contains obvious mesopores and the later contains additional micropores. Surface area and pore volume of mesopores (>2 nm) existing within the examined samples are also shown in Table 1. The samples with large surface areas show large pore volumes. Furthermore, most of the samples (Figure 4d,h and Figure 5b,c) show a broad size distribution ranging from several nanometers to decades of nanometers. Single size distributions centered at 14−16 nm are observed within the anatase nanocrystals (Figure 4e), and two types of size distribution centered at 3−5 and 14−16 nm are observed within the aligned nanorods (Figures 4c,f,g and 6b,a1,a2).

Optical Absorption Property of the TiO₂ Products. To determine the band gap, the absorption data shown in Figure 7 were fitted to the direct transition ($\alpha h\nu = A(h\nu - E_g)^{1/2}$) by extrapolating the linear portions of the curves to absorption equal to zero. In the equation, α is the absorption coefficient, $h\nu$ is the photo energy, E_g is the direct band gap, and A is a constant.[56] The calculated band gaps for the different TiO_2 products are shown in Figure 8. For concentrations <0.8 M, the band gap of the products obtained in all three acid solutions varies over a narrow range of 3.13−3.18 eV resulting from formation of the rutile phase. With increasing acid concentration, the band gap of the products prepared with HCl and HNO_3 rapidly increases to about 3.35 eV for those obtained in 0.8 M and about 3.34 eV for the products obtained in 1 M, respectively, and then decreases to about 3.1 eV for the products obtained in both 4.0 M HCl and HNO_3. The band gap of the TiO_2 products prepared in HNO_3 eventually levels off at around 3.1 eV for products obtained in 3.0−10 M. However, a continuous decrease in the band gap to 3.0 eV at 6 M is observed for the TiO_2products prepared in HCl. The observed variations in the band gap for the products prepared in HCl are caused by a rapid

decrease in the anatase content from 46% for 3 M to essentially zero at 6 M, but from 20% at 3 M to essentially zero at 8 M for the products prepared in HNO_3. In contrast, the band gap of the products prepared in H_2SO_4 exhibits a stable value of 3.12−3.18 eV for >0.9 M and then increases sharply to 3.29−3.34 eV for >2.0 M, which qualitatively agrees with the variation of the phase composition of the products, as seen in Figure 2.

Anatase and rutile are two most commonly encountered crystalline polymorphs. The absorption onset of anatase and rutile is around 387 (band gap energy, about 3.2 eV)[57] and 413 nm (band gap energy, about 3.0 eV),[58] respectively. The band gap of TiO_2 is determined by the positions of conduction band and valance band, which is adjustable by changing the crystal structure, phase composition, grain size, and morphology. The crystal structures of both anatase and rutile are made up of distorted TiO_6 octahedra, but in different ways. Rutile adopts a tetragonal structure (space group: D_{4h}^{14}), in which two opposing edges of each octahedron are shared to form linear chains along the [001] direction and the TiO_6 chains are then linked together via corner connection. Anatase (tetragonal, D_{4h}^{19}) has no corner sharing but has four edges shared per octahedron. The crystal structure of anatase can be viewed as zigzag chains of the octahedra linked together through edge sharing.[59] The valance band of anatase and rutile is mainly composed of O 2p states, while the conduction band is mainly formed of Ti 3d states.[60] Furthermore, the O 2p and Ti 3d hybridization is more covalent mixing in rutile than those in anatase. The valance band and the conduction band in anaase exhibits more pronounced O 2p and Ti 3d characters, respectively. Since the theoretical density for anatase is 3.84 $g \cdot cm^{-3}$, which is about 10% less than the 4.26 $g \cdot cm^{-3}$ for rutile, anatase thus has larger Ti−Ti distances than that of rutile, and it as a more pronounced localization of the Ti 3d states and a narrower 3d band. The photoexcited electron in anatase by UV excitation is less mobile than that generated in rutile.[61,62] In the present study, most of the TiO_2 products exhibit on average a relatively large grain size and thus no obvious blue shift is observed. The band gap of the mixture of anatase and rutile is between the values of pure anatase and rutile.

In a bulk semiconductor, an electron−hole pair is typically bound within a characteristic length called the Bohr exciton radius. If the electron and hole are constrained further, then the semiconductor's properties change. The quantum confined size of the nanocrystals is more significant at energies near the band
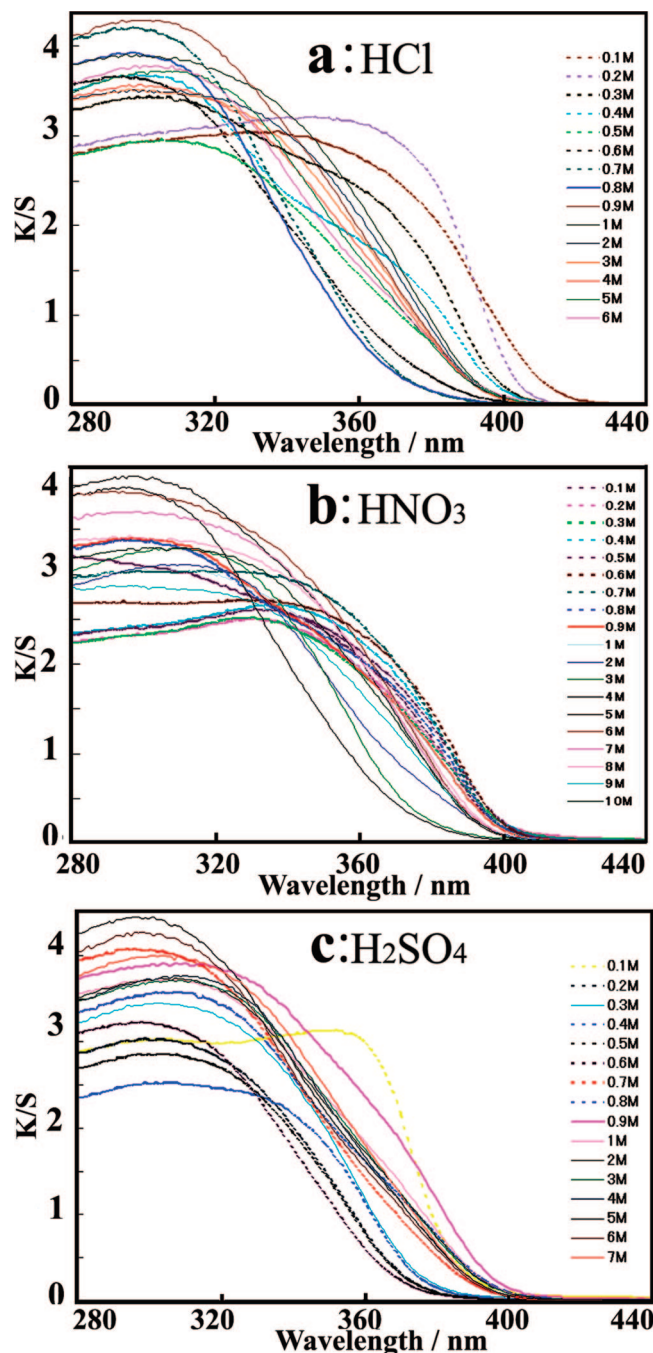
Hydrothermal Splitting of Titanate Fibers

J. Phys. Chem. C, Vol. 112, No. 24, 2008 **8815**

Figure 7. UV−vis DRS of the products hydrothermally synthesized with use of (a) HCl, (b) HNO$_3$, and (c) H$_2$SO$_4$, respectively.

Figure 8. Acid concentration dependence of the band gap of TiO$_2$ products hydrothermally synthesized with use of (a) HCl, (b) HNO$_3$ and (c) H$_2$SO$_4$, respectively.

gap. For the fluoresced light of nanocrystals, the nanocrystals with larger size emit light with lower energy, and thus display much redder. Conversely, the nanocrystals with small size emit light with higher energy, and thus display much bluer. The band gap energy that determines the energy of the fluoresced light is inversely proportional to the square of the size of the nanocrystals. Larger nanocrystals have more energy levels which are more closely spaced. This allows the nanocrystals to absorb photons containing less energy, i.e. those closer to the red end of the spectrum. The shape of the nanocrystals may well also be a factor in the quantum effect of the nanocrystals. In the present study, a blue shift is observed for the products consisting of fine nanocrystals with average grain sizes of around 15 nm (Figures 4e and 5c) or nanopores (Figure 6a1,a2), which can be due to the quantum effect.
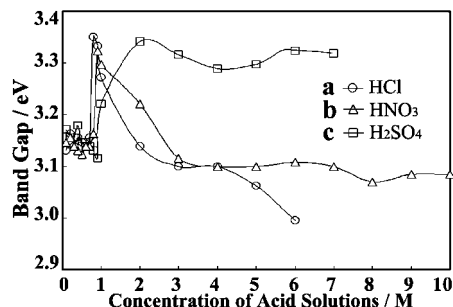
Furthermore, the surface defect of the nanocrystals increases with a decrease in the size of nanocrystals. Oxygen vacancies in the lattices have been widely observed within the TiO$_2$ nanocrystals. The electronic and optical properties of the TiO$_2$ nanocrystals can be altered considerably by oxygen defect structures created by the removal of oxygen atoms from the lattice.[63] Moreover, interface crystal lattice distortion has been reported to be important for the absorption edge shift toward the visible-light region.[64] Some samples, such as aligned rutile nanorods (Figure 4g,h), exhibit a red shift for band gap, which is due to oxygen vacancies or the interface crystal lattice distortion.

3.2. Shape and Structural Evolution of Aligned Rutile Nanorods and Anatase Nanocrystals. Hydrothermal synthesis has been widely used to prepare the anatase and rutile phases of TiO$_2$, using titanium precursors, such as TiCl$_4$, TiOSO$_4$, titanium isopropoxide, titanium acetylacetonate, etc. The crystalline phase of the product with use of these precursors is determined by the structure of the polymorphs and their organization during the nucleation process.[31–35] Generally, the initial hydrolysis of either Ti^{4+} or organic-protected Ti^{4+} under hydrothermal conditions results in the generation of dispersed octahedral [Ti(OH)$_2$(OH$_2$)$_4$]$^{2+}$ monomers or edge-sharing dimers that subsequently combine together through oxolation or olation, forming the initial nuclei at the reaction temperature. As the initial nuclei grow to exceed a critical size they become stable and further growth continues. During the formation of the initial nuclei, the [Ti(OH)$_2$(OH$_2$)$_4$]$^{2+}$ monomers can form different polymeric structures by sharing either equatorial (Figure 9a1) or apical edges (Figure 9a2). Considering the structures of the titania polymorphs, it is obvious that linear chains can only form rutile-type nuclei (Figure 9a1), while skewed chains are restricted to forming anatase-type nuclei (Figure 9a2). These nuclei then grow to form the rutile and anatase-type crystallites, respectively.

The basic crystal structure units of H$_2$Ti$_4$O$_9$·1.2H$_2$O fibers are [Ti$_4$O$_9$]$^{2-}$ sheets that are composed of four side-by-side aligned TiO$_6$ octahedra.[43–46,52,53] As shown in Figure 9b1,b2, the two central TiO$_6$ octahedra connect with the two adjacent TiO$_6$ octahedra by sharing two opposite equatorial edges of the octahedra at one level. The other two sides of the TiO$_6$ octahedra connect with the four TiO$_6$ octahedra units located at the same level by sharing the corners. The periodic repeating of such structure forms a single chain of TiO$_6$ octahedra. Furthermore, the four side-by-side aligned TiO$_6$ octahedra at different levels are connected above and below by sharing additional apical edges of TiO$_6$ octahedra, forming zigzag strings extending in the *b* direction, as well as the axial direction of H$_2$Ti$_4$O$_9$·1.2H$_2$O fibers. The protons and H$_3$O$^+$ ions are accommodated in the widely open interlayers of the layered framework of the
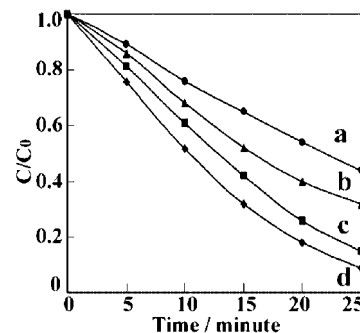
Figure 10. Photodegradation of methyl orange over (a) rutile shown in Figure 4h; (b) mixture of anatase and rutile shown in Figure 4f; (c) anatase shown in Figure 4e; and (d) P-25.

units of two the adjacent $[Ti_4O_9]^{2-}$ chains and along the connected corners of four-TiO_6 units of one chain, respectively, which are illustrated by Figure 9b3,b6.

By replacing protonic tetratitanate hydrate fibers with amorphous TiO_2 and other titanate hydrates, we have observed similar phase compositions depending on the nature and concentration of the acid. However, we have not observed a phase change when either crystalline anatase or rutile is used as a precursor. Therefore, the dehydration and the rearrangement of the crystal structure are two necessary steps involved in the acid-assisted hydrothermal route with amorphous TiO_2 and titanate hydrate precursors.

3.3. Photocatalytic Activity Evaluation of Various TiO_2 Nanocrytals and Nanostructures. To quantitatively evaluate the photodegradation of methyl orange, we studied its photodegradation kinetics over the different synthesized TiO_2 nanocrystalline samples and also Degussa P-25, which is widely used as a standard photocatalyst in photodegradation studies of the compound methyl orange. This helps reveal the influence of the individual catalysts on the reaction rate and evaluates their photocatalytic activities. However, the obtained information is only in reference to the apparent reaction kinetics since several processes contribute to the overall photodegradation of methyl orange. Figure 10 shows the typical temporal dependence of the photodegradation of methyl orange by UV light irradiation of the photocatalyst prepared with HCl. We have investigated the kinetics of methyl orange photodegradations over different samples and P-25 for quantitative evaluation of the activity of the samples, from which the apparent reaction rate constants have been calculated.[45,46]

The photodegradation kinetics of methyl orange in water is described according to the pseudo-first-order equation as given by the following:

$$r = -\frac{dC}{dt} = k_a t \tag{1}$$

where r is the reaction rate, C is the concentration of methyl orange in the solution, t is the reaction time, and k_a is the pseudo-first-order rate constant.

On the basis of data presented in Figure 10, by plotting $\ln(C_0/C)$ as a function of time t, through regression, we obtained for each sample the k (min^{-1}) constant from the slopes of the fitted straight lines. This linear relationship obeys the first-order reaction law that can be expressed by:

$$\ln(C_0/C) = kt \tag{2}$$

where C_0 (mgL^{-1}), C (mgL^{-1}), and k (min^{-1}) are the methyl orange initial concentration, the residual concentration at reaction time t, and the first-order rate constant, respectively. A higher

Figure 9. (a1, a2) Schematic representation of the nucleation and growth of anatase and rutile from octahedral cations formed by the hydrolysis of molecular titanium precursors; (b1, b3) schematic representation of the formation of rutile nanorods and anatase nanocrystals from protonic tetratitanate fibers under acid-assisted hydrothermal condition; (b1) protonic tetratitanate fibers growing along the *b* axis; (b2, b3) idealized crystal structure of layered protonic tetratitanate fibers and tunnel-structured octatitanate fibers, respectively, projected along the radial cross-section of fibers [● and ■, H_3O^+; ○ and □, H^+; ■ and □, H_3O^+ and H^+ at $y = 1/2$; ● and ○, H_3O^+ and H^+ at $y = 0$]; (b4) formation of rutile nanorods by breaking octatitanate structure along the connected corners of four TiO_6 units of two adjacent $[Ti_4O_9]^{2-}$ chains; (b5) formation of anatase nanocrystals by breaking the octatitanate structure along the connected corners of four-TiO_6 units of one chain; (b6) formation of the mixture of rutile nanorods and anatase nanocrystals.

$[Ti_4O_9]^{2-}$ sheets. During the dehydration processing, the structural water content is totally removed, and the $[Ti_4O_9]^{2-}$ sheets, each involving four octahedral TiO_6 units, shift with respect to each other in the amount of $\bar{C}/4$ in the structure of $H_2Ti_4O_9 \cdot 1.2H_2O$. They share free corners of four-TiO_6 units and gradually condense with each other to form an octatitanate with a tunnel-like crystal structure. Half of the oxygen located at the free corner of the four-TiO_6 unit is removed by combining with the two H^+ located at the exterior of the four-TiO_6 unit to form H_2O. Both the anatase and rutile phases are able to be formed from the tunnel-structured octatitanate fibers by dehydration and condensation of the $[Ti_4O_9]^{2-}$ sheets. As described above, the crystal growth units of rutile and anatase are linear chains and skewed chains, respectively. Therefore, the split of the octatitanate structure to from rutile nanorods and anatase nanocrystals is along the connected corners of the four-TiO_6

value of the constant k for a particular catalyst means that it has a higher activity for photodegradation of methyl orange, which allows us to quantitatively determine the photocatalytic activities of the different catalysts.

The regression results of the k values for the samples with different phase structures, morphologies, and microstructures are summarized in Table 1. As seen in Table 1, the k value decreases in going from anatase (Figures 4e and 6a1,a2), to a mixture of rutile and anatase (Figures 4d,f, 5b,c, and 6b), and to the rutile phase (Figure 4c,g,h). For the products of pure rutile phase, aligned nanoporous rutile nanorods (Figure 4h) exhibit the highest value of k among all the rutile products (Figure 4c,g). For the products of mixed rutile and anatase, the value of k increases with increasing anatase content. For the products of the pure anatase phase, the anatase nanocrystals (Figure 4e) exhibit a k value of 0.078, which is somewhat higher than the value 0.071 obtained for nanoporous nanorods (Figure 6a1,a2). The standard P-25 sample exhibits the highest k value as compared to those of all the prepared samples.

The surface areas and pore properties are other key factors that influence both the activity of photocatalysts and the efficiency of photocatalytic reactions. For typical samples, their BET specific surface area, micropore (<1 nm) surface area, and mesopore (>2 nm) surface area and pore volume are shown in Table 1. The larger the surface area of the sample is, the higher the photocatalytic activity of the sample is. However, some samples exhibit very large surface areas, such as the mixture of aligned rutile nanorods and anatase nanocrystals (Figure 6b), but their photocatalytic activity is still lower than those of anatase nanocrystals (Figure 4e), aligned nanoporous anatase nanorods (Figure 6a1,a2), and P-25, which indicates that the phase structure and phase composition of the TiO_2 photocatalysts are the primary factor in controlling the photocatalytic activity of TiO_2 photocatalysts.

We had previously reported the synthesis of novel nanostructured porous fibers of self-supported, radially aligned $H_2Ti_8O_{17}\cdot1.5H_2O$ nanorods that are prepared from the layered $H_2Ti_4O_9\cdot1.2H_2O$ fibers by solvothermal reaction in glycerine. They exhibited high photooxidative activity, superior to that of P-25.[45,46] However, a decrease in the photocatalytic activity was observed after three cycles, which renders them unsuitable for long-term photocatalytic applications. In the present work, we have demonstrated a novel inorganic acid-assisted hydrothermal route for the preparation of single-crystalline TiO_2 nanostructures with controllable crystalline phase, morphology, and microstructures using protonic tetratitanate hydrate fibers as a cheap and stable synthetic precursor. As shown in Table 1, the apparent photocatalytic reaction rate constants of some of the samples (Figures 4e and 6a1,a2) are close to that of P-25. More importantly, the photocatalytic activities of these samples are stable with time, which makes them useful for long-term photocatalytic applications. We believe that the systematically controlled materials properties, such as crystalline phase, morphology, and microstructure, of these single-crystalline TiO_2 nanostructures make them useful for a wide range of potential applications in photocatalysis, environmental pollution control, and solar energy conversion.

References and Notes

(1) Salbeck, J.; Spreitzer, H.; Gratzel, M. *Nature* **1998**, *395*, 583.
(2) O'Regan, B.; Gratzel, M. *Nature* **1991**, *353*, 737.
(3) Fox, M. A.; Dulay, M. *Chem. Rev.* **1995**, *93*, 341.
(4) Linsebigler, A. L.; Lu, G.; Yates, J. T., Jr *Chem. Rev* **1995**, *95*, 735.
(5) Naumov, I. I.; Bellaiche, L.; Fu, H. *Nature* **2004**, *432*, 737.
(6) Huang, M. H.; Mao, S.; Feick, H.; Yan, H.; Wu, Y.; Kind, H.; Weber, E.; Russo, R.; Yang, P. *Science* **2001**, *292*, 1897.
(7) Peng, X.; Manna, L.; Yang, W.; Wickham, J.; Scher, E.; Kadavanich, A.; Alivisatos, A. P. *Nature* **2000**, *404*, 59.
(8) Shen, L.; Bao, N.; Yanagisawa, K.; Zheng, Y.; Domen, K.; Gupta, A.; Grimes, C. A. *J. Solid State Chem.* **2007**, *180*, 213.
(9) Shen, L.; Bao, N.; Yanagisawa, K.; Domen, K.; Grimes, C. A.; Gupta, A. *J. Phys. Chem. C* **2007**, *111*, 7280.
(10) Law, M.; Greene, L. E.; Johnson, J. C.; Saykally, R.; Yang, P. D. *Nat. Mater.* **2005**, *4*, 455.
(11) Wells, A. F. *Structural Inorganic Chemistry*; Clarendon Press: Oxford, UK, 1975.
(12) Shannon, R. D.; Pask, J. A. *J. Am. Ceram. Soc.* **1965**, *48*, 391.
(13) Fahmi, A.; Minot, C.; Silvi, B.; Causá, M. *Phys. Rev. B* **1993**, *47*, 11717.
(14) Kim, K. J.; Benksten, K. D.; van de Lagemaat, J.; Frank, A. J. *Chem. Mater.* **2002**, *14*, 1042.
(15) Fujishima, A.; Rao, T. N.; Tryk, D. A. *J. Photochem. Photobiol. A* **2000**, *1*, 1.
(16) Yamabi, S.; Imai, H. *Chem. Mater.* **2002**, *14*, 609.
(17) Khan, S. U. M.; Al-Shahry, M.; Ingler, W. B. *Science* **2002**, *297*, 2243.
(18) Burda, C.; Chen, X.; Narayanan, R.; El-Sayed, M. A. *Chem. Rev.* **2005**, *105*, 1025.
(19) Hulteen, J. C.; Martin, C. R. *J. Mater. Chem.* **1997**, *7*, 1075.
(20) Gong, D.; Grimes, C. A.; Varghese, O. K.; Hu, W.; Singh, R. S.; Chen, Z.; Dickey, E. C. *J. Mater. Res.* **2001**, *16*, 3331.
(21) Ghicov, A.; Macak, J. M.; Tsuchiya, H.; Kunze, J.; Haeublein, W.; Frey, L.; Schmuki, P. *Nano. Lett* **2006**, *6*, 1080.
(22) Limmer, S. J.; Seraji, S.; Wu, Y.; Chou, T. P.; Nguyen, C.; Cao, G. *Adv. Funct. Mater.* **2002**, *12*, 59.
(23) Kanie, K.; Sugimoto, T. *Chem. Commun.* **2004**, 1584.
(24) Xu, N.; Shi, Z.; Fan, Y.; Dong, J.; Shi, J.; Hu, M. *Ind. Eng. Chem. Res.* **1999**, *38*, 373.
(25) Wang, C.; Ying, J. Y. *Chem. Mater.* **1999**, *11*, 3113.
(26) Li, G.; Li, L.; Boerio-Goates, J.; Woodfield, B. F. *J. Am. Chem. Soc.* **2005**, *127*, 8659.
(27) Yanagisawa, K.; Ovenstone, J. *J. Phys. Chem. B* **1999**, *103*, 7781.
(28) Ovenstone, J.; Yanagisawa, K. *Chem. Mater.* **1999**, *11*, 2770.
(29) Wang, C.; Ying, J. Y. *Chem. Mater.* **1999**, *11*, 3113.
(30) Zhang, Z.; Wang, C. C.; Zakaria, R.; Ying, J. Y. *J. Phys. Chem. B* **1998**, *102*, 10871.
(31) Hosono, E.; Fujihara, S.; Kakiuchi, K.; Imai, H. *J. Am. Chem. Soc.* **2004**, *126*, 7790.
(32) Zheng, Y.; Shi, E.; Chen, Z.; Li, W.; Hu, X. *J. Mater. Chem.* **2001**, *11*, 1547.
(33) Zheng, Y. Ph.D. Dissertation, Chapters 3 and 4 (Investigation on the Growth Mechanism of Polymorphs in Low Restricted System), Shanghai Institute of Ceramics, Chinese Academy of Sciences, China.
(34) Yin, H.; Wada, Y.; Kitamura, T.; Kambe, S.; Murasawa, S.; Mori, H.; Sakata, T.; Yanagida, S. *J. Mater. Chem.* **2001**, *11*, 1694.
(35) Yamabi, S.; Imai, H. *Chem. Mater.* **2002**, *14*, 609.
(36) Trentler, T. J.; Denler, T. E.; Bertone, J. F.; Agrawal, A.; Colvin, V. L. *J. Am. Chem. Soc.* **1999**, *121*, 1613.
(37) Lencka, M. M.; Riman, R. E. *J. Am. Ceram. Soc.* **1993**, *76*, 2649.
(38) Lencka, M. M.; Anderko, A.; Riman, R. E. *J. Am. Ceram. Soc.* **1995**, *78*, 2609.
(39) Lencka, M. M.; Oledzka, M.; Riman, R. E. *Chem. Mater.* **2000**, *12*, 1323.
(40) Bao, N.; Feng, X.; Shen, L.; Lu, X. *Cryst. Growth Des.* **2002**, *2*, 437.
(41) Bao, N.; Shen, L.; Feng, X.; Lu, X. *J. Am. Ceram. Soc.* **2004**, *87*, 326.
(42) Bao, N.; Feng, X.; Lu, X.; Shen, L.; Yanagisawa, K. *AIChE, J.* **2004**, *50*, 1568.
(43) Sasaki, T.; Watanabe, M.; Fujiki, Y.; Kitami, Y. *Chem. Mater.* **1994**, *6*, 1749.
(44) Yin, S.; Sato, T. *Ind. Eng. Chem. Res.* **2000**, *39*, 4526.
(45) Bao, N.; Shen, L.; Yanagisawa, K. *J. Phys. Chem B* **2004**, *108*, 16739.
(46) Bao, N.; Feng, X.; Yang, Z.; Shen, L.; Lu, X. *Environ. Sci. Technol.* **2004**, *38*, 2729.
(47) Feng, Q.; Hirasawa, M.; Yanagisawa, K. *Chem. Mater.* **2001**, *13*, 290.

8818 *J. Phys. Chem. C, Vol. 112, No. 24, 2008*

Shen et al.

(48) Ohara, Y.; Koumoto, K.; Yanagid, H. *J. Am. Ceram. Soc.* **1994**, *77*, 2327.

(49) Feng, Q.; Hirasawa, M.; Kajiyoshi, K.; Yanagisawa, K. *J. Am. Ceram. Soc.* **2005**, *88*, 1415.

(50) Bao, N.; Feng, X.; Lu, X.; Yang, Z. *J. Mater. Sci.* **2002**, *37*, 3035.

(51) Bao, N.; Lu, X.; Ji, X.; Xie, J. *Fluid Phase Equilib.* **2002**, *193*, 229.

(52) Izawa, H.; Kikkawa, S.; Koizumi, M. *J. Phys. Chem.* **1982**, *86*, 5023.

(53) Sasaki, T.; Watanabe, M.; Komatsu, Y.; Fujiki, Y. *Inorg. Chem.* **1985**, *24*, 2265.

(54) Klug, H. P.; Alexander, L. E. *X-ray Diffraction Procedures for Polycrystalline and Amorphous Materials*, 1st ed.; Wiley: New York, 1954; Chapter 19.

(55) Shen, L.; Bao, N.; Yanagisawa, K.; Domen, K.; Gupta, A.; Grimes, C. A. *Nanotechnology* **2006**, *17*, 5117.

(56) Bao, N.; Shen, L.; Takata, T.; Domen, K.; Gupta, A.; Yanagisawa, K.; Grimes, A. C. *J. Phys. Chem. C* **2007**, *111*, 17527.

(57) Tang, H.; Levy, F.; Berger, H.; Schmid, P. E. *Phys. Rev. B* **1995**, *52*, 7771.

(58) Arntz, F.; Yacoby, Y. *Phys. Rev. Lett.* **1966**, *17*, 857.

(59) Daude, N.; Gout, C.; Jouanin, C. *Phys. Rev. B* **1977**, *15*, 3229.

(60) Wells, A. F. *Structural Inorganic Chemistry*, 5th ed.; Claredon Press: Oxford, UK, 1984.

(61) Asahi, R.; Taga, Y. *Phys. Rev. B* **2000**, *61*, 7459.

(62) Valentin, C. D.; Pacchioni, G.; Selloni, A. *Phys. Rev. B* **2004**, *70*, 085116.

(63) Oertzena, G. U.; Gerson, A. R. *J. Phys. Chem. Solids* **2007**, *68*, 324.

(64) Ye, J.; Zou, Z. *J. Phys. Chem. Solids* **2005**, *66*, 266.